Numerical Simulations of Subsonic and Transonic Open-Cavity Flows

Yiyang Sun[*], Aditya G. Nair[†], Kunihiko Taira[‡], Louis N. Cattafesta[§]
Florida State University, Tallahassee, FL

Guillaume A. Brès[¶]
Cascade Technologies, Inc., Palo Alto, CA

Lawrence S. Ukeiley[‖]
University of Florida, Gainesville, FL

Two-dimensional open-cavity flows for free stream Mach number of 0.1 to 1.6 are investigated with direct numerical simulations for cavities of aspect ratio 2 and 6 to characterize the flow stability. We determine the neutral stability curve over a wide range of Mach numbers and Reynolds numbers. In particular, we examine the effects of compressibility on the flow in transonic regime at low Reynolds numbers. Rossiter modes are identified by spectral analysis. The corresponding spatial structures associated with the dominant and subdominant Rossiter modes are extracted with dynamic mode decomposition. The nature of these structures provides us insight to their contribution to instability of the flow. The interaction between the shock waves and the shear layer modes for the transonic flows are investigated.

I. Introduction

Understanding the fundamental problem of flow over open cavities can provide insights into the behavior of the flow over sunroofs, landing gear wells, gaps, and weapon bays. Instabilities can develop in the shear layer that convects over the cavity and may develop into self-sustained oscillations. The perturbation in the shear layer grows, convects downstream and impinges on the cavity trailing edge, which generates acoustic waves that propagate upstream to provide a natural feedback loop. The early work of Rossiter predicts the two-dimensional shear-layer oscillation frequency through a semi-empirical formula as a function of the free stream Mach number.[1] The mode corresponding to this frequency is referred to as the Rossiter mode. Since then, there has been a large number of experimental and numerical studies performed to examine the influence of Reynolds number and cavity geometry on the oscillations of the flow.[2,3]

The aerodynamic and acoustic fluctuations created from the flow over cavity can lead to airframe and store damage as well as high-level noise emission. In order to mitigate such fluctuations, active flow control strategies have been used to alter the flow field. Both open and closed loop control techniques have demonstrated the ability to significantly reduce the pressure fluctuations and noise.[4,5] However, effective control at transonic and supersonic flow conditions remains an elusive goal. The present numerical investigation aims to

[*]Graduate Research Assistant, Department of Mechanical Engineering and Florida Center for Advanced Aero-Propulsion, ys12d@my.fsu.edu.

[†]Graduate Research Assistant, Department of Mechanical Engineering and Florida Center for Advanced Aero-Propulsion, agn13@my.fsu.edu.

[‡]Assistant Professor, Department of Mechanical Engineering and Florida Center for Advanced Aero-Propulsion, ktaira@fsu.edu.

[§]Eminent Scholar and Professor, Department of Mechanical Engineering and Florida Center for Advanced Aero-Propulsion, lcattafesta@fsu.edu.

[¶]Senior Research Scientist, gbres@cascadetechnologies.com.

[‖]Associate Professor, Department of Mechanical and Aerospace Engineering and Florida Center for Advanced Aero-Propulsion, ukeiley@ufl.edu.

uncover the inherent hydrodynamic instability in cavity flows such that effective flow control techniques can be adapted. The overall goal is to develop a three-dimensional flow control methodology in the range of Mach numbers from 0.6 to 1.6. As the first step towards this goal, we extend the stability analysis[6] performed on open cavity for subsonic flow[7,8] to transonic flow considering the effects of Reynolds number, Mach number and cavity aspect ratio. Our intention here is to perform a two-dimensional characterization of the cavity flow to distinguish between stable and unstable cases utilizing nonlinear simulations. We apply dynamic mode decomposition[9] techniques to the unstable cases to gain insight into the dominant flow physics. The findings from this study help serve as a foundation to extract a two-dimensional base state as input for bi-global stability analysis in order to uncover three-dimensional instabilities. The present analysis will be invaluable for design of efficient and effective three-dimensional flow control inputs to mitigate fluctuations.

In what follows, we present the computational approach with its validation in §II. In §III, we discuss our findings on the two-dimensional stability characteristics over a wide range of Reynolds number and Mach number with aspect ratio 2 and 6. The flow field is further examined through the use of the dynamic mode decomposition to extract the temporal and spatial properties of the flow instabilities.

II. Simulation Approach

A. Computational Setup

The high-fidelity compressible flow solver *CharLES*[10] developed by Cascade Technologies is used to solve the full compressible Navier–Stokes (NS) equations and study the open-cavity flows. The spatial coordinate x, time t, density ρ, velocity $\mathbf{u}$, energy e, pressure P, temperature T, are non-dimensionalized with respect to freestream conditions and cavity depth D as

$$x_i = \frac{{x_i}^d}{D}, \qquad t = \frac{t^d a_\infty}{D}, \qquad \rho = \frac{\rho^d}{\rho_\infty}, \qquad \mathbf{u} = \frac{\mathbf{u}^d}{a_\infty},$$
$$e = \frac{e^d}{\rho_\infty a_\infty^2}, \qquad P = \frac{P^d}{\gamma P_\infty}, \qquad T = \frac{T^d}{T_\infty},$$

where variables with superscript d refer to the dimensional quantities and those with the subscript ∞ denotes the freestream parameters. The ratio of specific heats γ and total energy e are given by $\gamma = c_p/c_v$ and $e = \rho(E + |\mathbf{u}|^2/2)$, respectively, where E is the internal energy per unit mass. The Prandtl number Pr and Reynolds number Re_D (based on cavity depth) are defined as

$$Pr = \frac{c_p \mu_\infty}{k}, \qquad Re_D = \frac{\rho_\infty U_\infty D}{\mu_\infty},$$

where k is the thermal conductivity and μ_∞ is freestream dynamic viscosity.

No sub-grid scale modeling is used for the simulations considered in this work. A structured mesh with non-uniform spacing in both x- and y-directions is used for the two-dimensional simulations. The open-cavity flows are specified with cavity aspect ratio (L/D), where L and D represent the length and depth of cavity, respectively, initial boundary layer momentum thickness (θ_0) at the leading edge of the cavity, the ratio of the cavity depth to the initial momentum thickness (D/θ_0) and Reynolds number (Re_D). We also define a Reynolds number based on the initial momentum thickness ($Re_\theta \equiv \rho_\infty U_\infty \theta_0/\mu_\infty$).

In the present investigation, we consider the cavity geometries with aspect ratios of $L/D = 2$ and 6. The computational setup for $L/D = 2$ is illustrated in Figure 1. The setup for $L/D = 6$ has a similar configuration. The computational domain consists of the leading edge of cavity located at the origin $(0, 0)$ of the Cartesian coordinate system with the x-direction representing the streamwise direction in the flow field. In order to prescribe the initial momentum boundary layer thickness at the leading edge of the cavity, the length of floor upstream of cavity is varied from $2.4D$ (for lower Re_θ) to $5D$ (for higher Re_θ). The downstream floor length is fixed at $7D$ while the normal distance from cavity surface to top boundary of domain is maintained at $9D$.

We study the effects of Mach number from the subsonic regime ($0.1 \leq M_\infty \leq 0.8$) to the transonic regime ($0.8 \leq M_\infty \leq 1.6$), with Re_D varying from 100 to 3800 for cavity aspect ratios of $L/D = 2$ and 6. The wide range of Reynolds numbers and Mach numbers enables us to characterize their effects on the flow field. The ratio of the cavity depth to the initial momentum thickness D/θ_0 is maintained to be constant for all the cases considered, as described below. To initialize the flow field, we use the incompressible Blasius

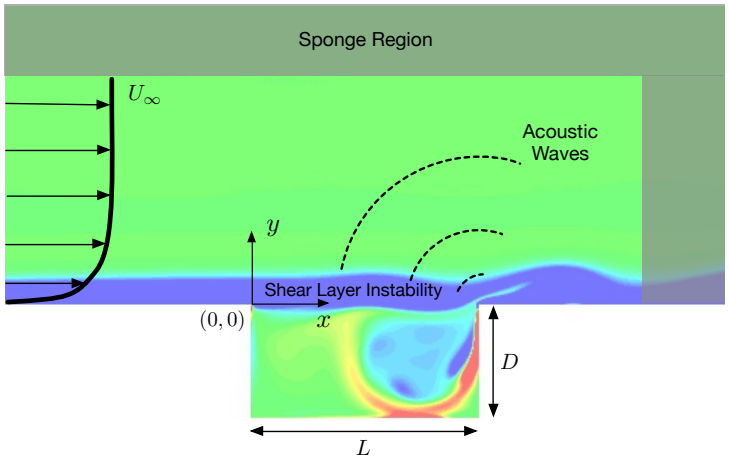

Figure 1: Computational configuration for open cavity flow (not to scale).

boundary layer profile over the computational domain with free stream velocity U_∞ and set the flow to be quiescent inside the cavity. The same profile is used at the inlet of the cavity for $L/D = 2$. The variation in boundary layer thickness for the range for Mach number from 0 to 1.4 is less than 10 percent.[11] Because this change is relatively small, the incompressible Blasius boundary layer profile is utilized. Furthermore, in order to validate the use of the incompressible boundary layer profile, we compare the profile to the results of the full compressible NS equations on a flat plate. Both results obtained with the incompressible and compressible boundary layer profiles match with reasonable accuracy. As the Blasius profile is characterized by the momentum boundary layer thickness, we fix $D/\theta_0 = 26.4$ for all the cases considered. This constraint helps in observing the effects of Mach number, Reynolds number and cavity geometry parameterized by momentum boundary layer thickness.

In order to study the effects of cavity aspect ratio on flow instabilities, for $L/D = 6$ cases, the upstream floor length is varied to satisfy the desired momentum thickness at cavity leading edge specifying different Re_θ. We primarily consider low Reynolds number cases for $L/D = 6$. Lower Reynolds numbers leads to the specification of shorter startup length upstream of the cavity for boundary layer to develop. No-slip and iso-thermal boundary conditions are specified at the upstream and downstream floor as well as the wall of the cavity. To damp out the existing acoustic waves and wake structures, sponge zones are applied along the outlet and top boundaries with a length of $2D$ from computational boundaries.[12]

B. Validation

We perform a grid convergence study for both cavity aspect ratios considered in the present work, to determine the grid resolution necessary to perform the direct numerical simulations. A Reynolds number $Re_\theta = 104$ ($Re_D = 2746$) and $M_\infty = 0.2$ for $L/D = 2$, and $Re_\theta = 46$ ($Re_D = 1214$) and $M_\infty = 0.6$ for $L/D = 6$ are considered for performing grid convergence study. The baseline computation is performed on a structured mesh with approximately a half million grid points. A finer mesh with one million grid points is chosen for comparison with the baseline case. The comparison of the v velocity history at the midpoint location ($x = L/2$ and $y = 0$) over the cavity is shown in Figure 2. The results from the two grids are nearly identical exhibiting sufficient grid resolution in terms of grid convergence. A higher Reynolds number $Re_\theta = 144$ was also considered for $L/D = 2$ to validate the grid convergence study. The baseline grid of half million grid points is proved sufficient to achieve reasonable grid resolution even for higher Reynolds numbers. We compare our results for instantaneous dilatation in cavity for $L/D = 2$, $D/\theta_0 = 26.4$, $M_\infty = 0.6$, $Re_\theta = 56.8$ ($Re_D = 1500$) with the numerical Schlieren by Brès[13] for the same setup, as shown in Figure 3 with qualitative agreement.

In the cases considered, we observe the trend for the resonant frequency predicted by the Rossiter's semi-empirical formula given by

$$St_n = \frac{n - \alpha}{M_\infty + 1/\kappa},$$

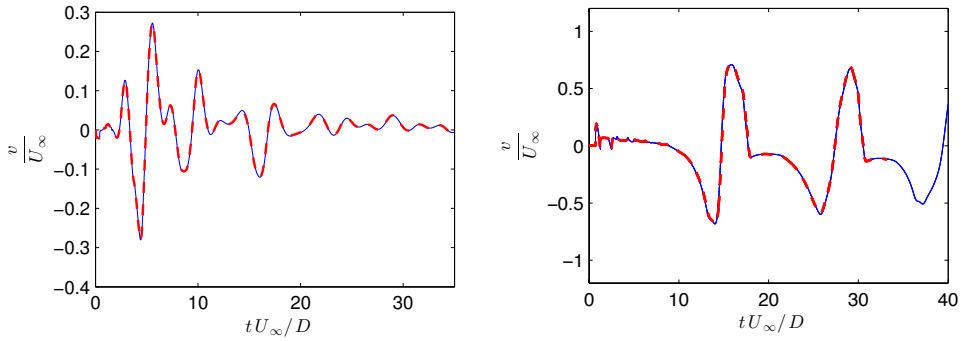

Figure 2: Comparison of the v-velocity at the midpoint ($x = L/2$, $y = 0$) of the open cavity. Blue solid line is the baseline case with half million grid points and red dash line is the refined case with 1.1 million grid points. Left: $L/D = 2$. Right: $L/D = 6$.

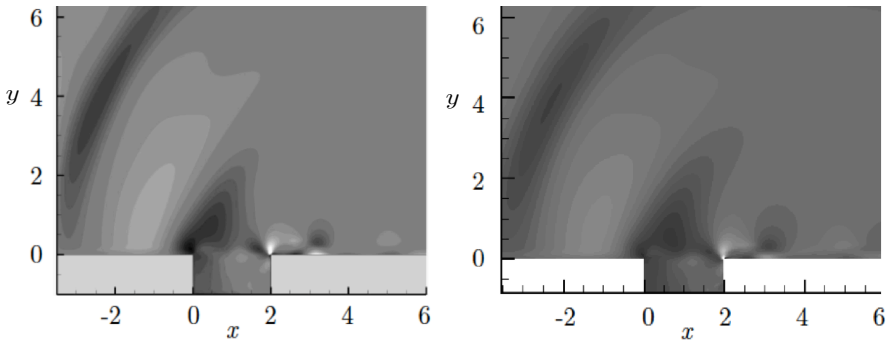

Figure 3: Comparison of the numerical Schlieren from the direct numerical simulation by Brès[13] (left) and the present work (right) at $M_\infty = 0.6$.

where M_∞ represents freestream Mach number, empirical constant κ (≈ 0.57) is the average convective speed of disturbance in shear layer, α ($= 0.25$) corresponds to phase delay, and $n = 1, 2, \ldots$ leads to the nth Rossiter mode. The accuracy of the original formula decreases when $M_\infty > 1.4$. The modified version is given by Heller et al[14] as

$$St_n = \frac{n - \alpha}{\frac{M_\infty}{\sqrt{1+\frac{\gamma-1}{2}M_\infty^2}} + 1/\kappa},$$

where γ ($= 1.4$) is the ratio of specific heats and other parameters are the same as original one described above. We compare our results with frequency prediction based on these formulas and find the present results agree well with those of others.

In addition, we carry out computations for Mach numbers of $M_\infty = 0.8$ and 1.4 and compare the results with Schlieren images of Krishnamurty[15] and numerical results of Rowley.[16] In the experiments conducted by Krishnamurty,[15] the cavity depth is 0.1 inch with $L/D = 2$ and the width is almost 40 times the depth ($W/D \approx 40$). Hence, the results from this experimental study can be treated as approximately two-dimensional. We maintain a similar setup for the parameters involved except that the Reynolds number of the experiments conducted by Krishnamurty[15] is five times higher. We can observe the gradient of density in x-direction of instantaneous acoustic field in Figure 4. The density gradient exhibits good agreement with experiments and the simulation results. For $M_\infty = 0.8$, the acoustic waves generated at the trailing edge of cavity propagate upstream, but for the $M_\infty = 1.4$ case, the acoustic wave structures are inclined in the

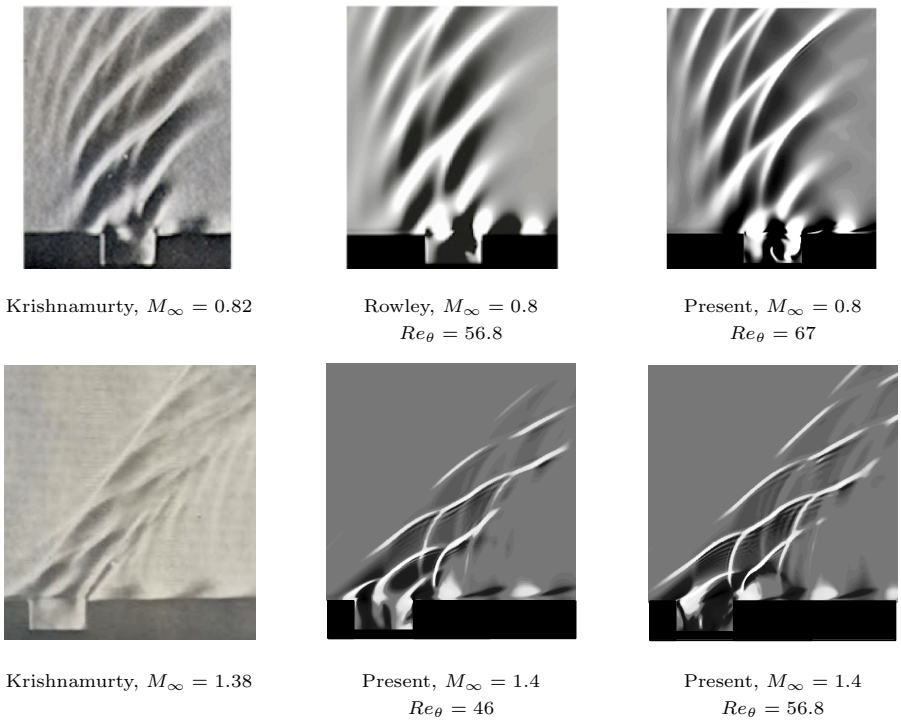

Figure 4: Comparison of Schlieren images by Krishnamurty[15] and the direct numerical simulation by Rowley[16] with the present work ($\partial\rho/\partial x$) at $M_\infty = 0.8$ and 1.4.

streamwise direction. Further analysis of the higher Mach number cases are provided in §III.

III. Results

To understand how a self-sustained open-cavity flow oscillation is triggered, the present studies focus on examining the effects of Re, L/D, Mach number and D/θ_0. These parameters are widely discussed in previous literatures and show significant effects on cavity flow modes. In our work, D/θ_0 is fixed in all the cases considered and the effects of the individual parameters are studied by changing them one at a time. We expand our studies to subsonic ($M_\infty < 0.2$), with M_∞ lower than those considered by Brès,[13] and transonic regimes ($0.7 < M_\infty < 1.6$). The interactions between shock waves and the shear layer are captured and compressibility effects are analyzed. Extensive simulations are performed to understand the behavior of the Rossiter modes with large M_∞ and Re_θ around the transitional zone between stable and unstable flow. Cases considered in the present study are summarized in Table 1 and 2 in the appendix.

A. Flow over cavity of $L/D = 2$

For $L/D = 2$, we perform direct numerical simulation on a number of cases that span the range of Mach numbers from $M_\infty = 0.1$ to 1.6 and Reynolds number (Re_D) up to 3800. The parameters of M_∞ and Re_D are chosen to expand upon the stability analysis performed by Brès and Colonius.[8] We extend their analysis to lower and higher Mach number regimes. Furthermore, extensive simulations have been performed to extract the modal characteristics with fixed Mach numbers and varying Reynolds number and vice versa.

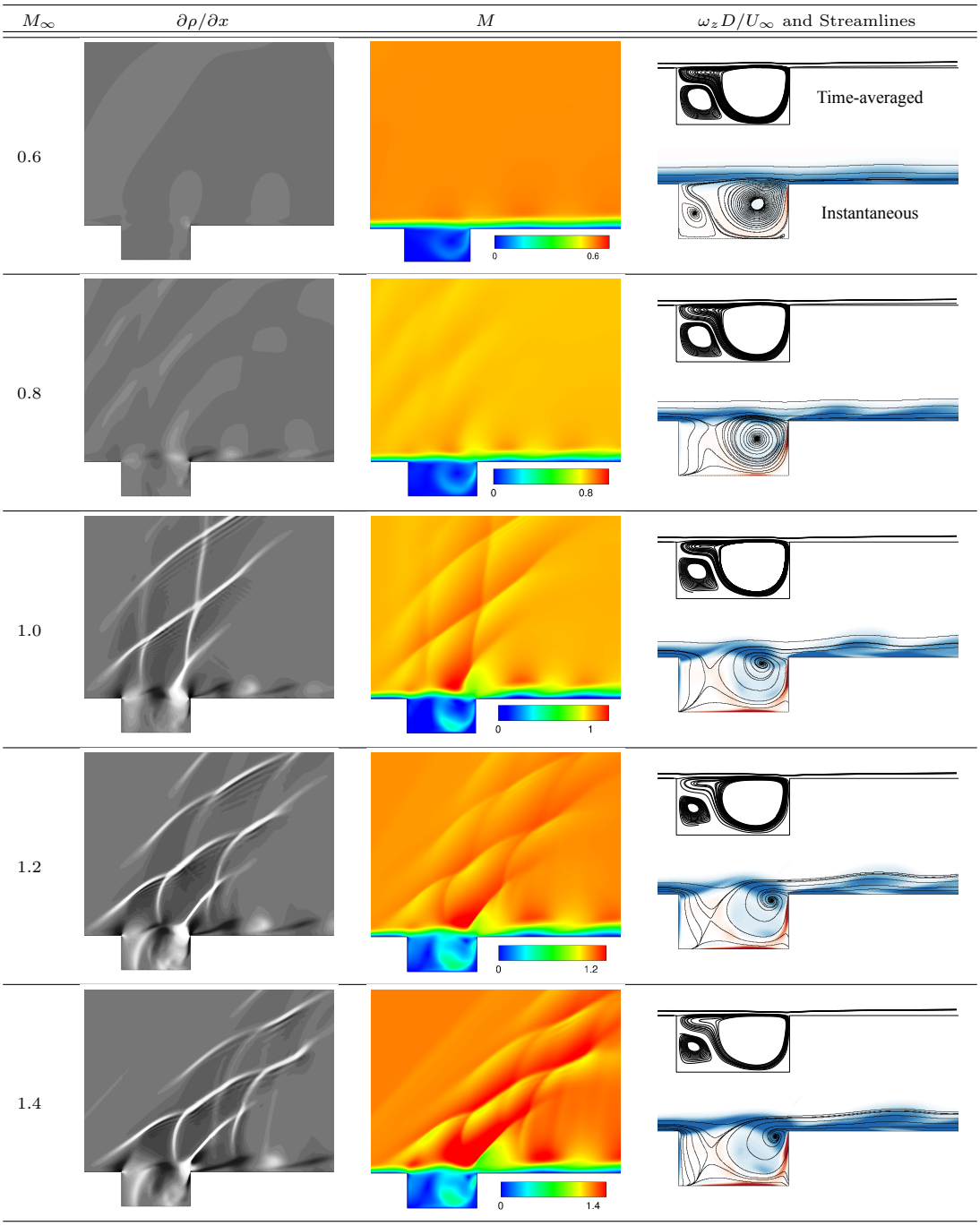

Figure 5: Numerical Schilieren ($\partial\rho/\partial x$, instantaneous), local Mach number (M, instantaneous) and vorticity ($\omega_z D/U_\infty$, instantaneous and time-averaged) contours are shown for $M_\infty = 0.6$ to 1.4 and $L/D = 2$ at $Re_\theta = 46$ ($Re_D = 1214$).

To examine how shear layer modes affect the acoustic emission at the trailing edge of cavity, the density gradient fields for Mach numbers of 0.6 to 1.4 are shown in Figure 5 at $Re_\theta = 46$. In the present work with $L/D = 2$, we only observe the shear layer mode. The shear layer over the cavity rolls up and hits the trailing edge periodically and acoustic waves are emitted and propagated into the flow. The density gradient in x-direction shown in the first column is plotted with same contour levels from -0.8 to 0.8. From the flow field, we can observe the density fluctuation caused by self-sustained oscillations. When free stream Mach number increases to 0.8, the acoustic radiation emitted from the trailing edge becomes stronger and the wavelength becomes smaller, which is also observed and discussed by Rowley.[16] However, when $M_\infty \geq 1.0$, the acoustic

field becomes more intense and its structure appears clearly directional. This phenomenon is also noticed in experiments by Krishnamurty.[15] The local Mach number changes from M_∞ outside the cavity to subsonic speeds within the cavity. The compression wave generated at the rear corner propagates upstream and is reflected from the front wall, which forms a cycle inside the cavity. When it propagates upstream outside of the cavity, it is swept by the oncoming supersonic flow, which is why we observe the bent compression waves propagating downstream. Meanwhile, at the leading edge of cavity, shear layer oscillation leads to periodic expansion and compression waves in the supersonic flow. These waves propagating upstream are also swept by the oncoming supersonic flow with small part of compression ahead of the leading edge. Furthermore, a Mach wave is formed with an angle of $\sin^{-1}(1/M_\infty)$. At the trailing edge, for the oncoming flow with a large deflection angle, a bow shock is formed due to the impingement of the shear layer on the trailing edge.

For all cases considered for the cavity of $L/D = 2$, we record the velocity v/U_∞ time history of the point located in the middle of the cavity shear layer ($x = L/2$, $y = 0$). We perform Fourier transform (spectral analysis) on probe data which is collected after a minimum of 50 convective units to flush out the transients. The simulations are conducted long enough to observe the nature of oscillations in the nonlinear regime. If all oscillations decay over time, we infer that the system is stable. For the unstable cases, we extract oscillation frequencies nondimensionalized by $St_L = fL/U_\infty$ and compare them with Rossiter's prediction. The expression of semi-empirical Rossiter formula is independent of Re number, which suggests that Mach number is the primary variable that influences the oscillation frequency. For a fixed Re_θ, Strouhal number shows a decreasing trend with increasing M_∞ as represented in Figure 6.

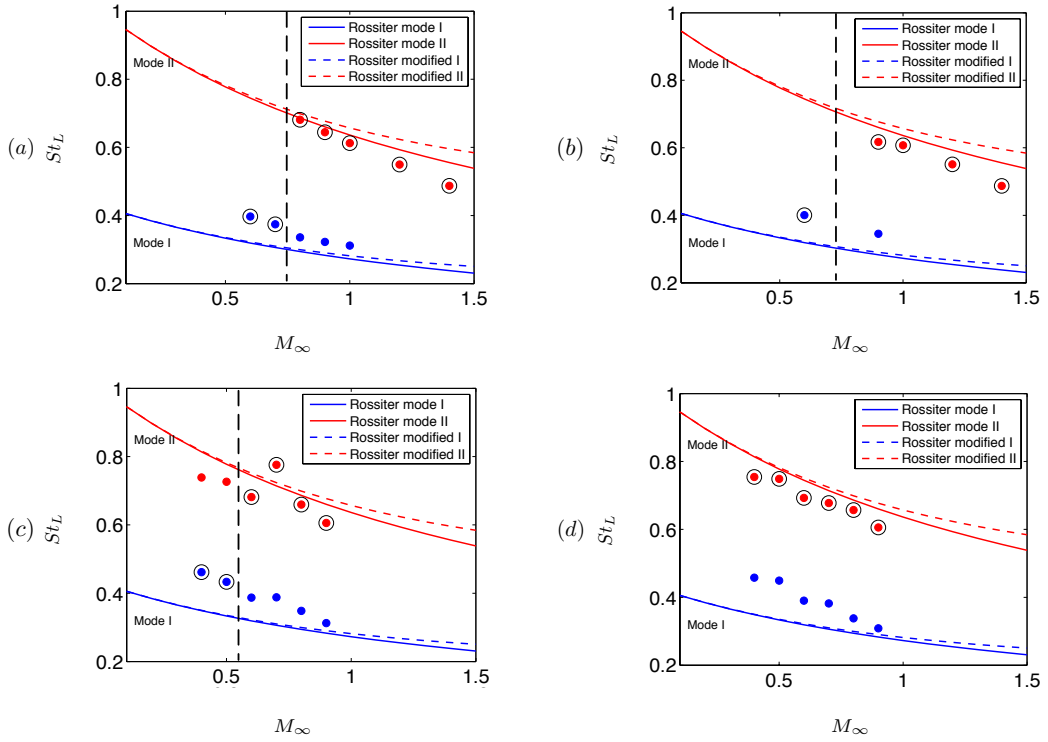

Figure 6: Comparison of $St_L = fL/U_\infty$ from classic Rossiter semi-empirical formula (solid line), modified Rossiter formula (dashed line) and present work for (a) $Re_\theta = 46$; (b) $Re_\theta = 56.8$; (c) $Re_\theta = 67$; (d) $Re_\theta = 77$. The blue and red symbols and lines represent frequencies corresponding to Rossiter mode I and II, respectively. Rossiter mode I and II are dominant on the left and right side of the black dashed line, respectively, indicated by black open circles.

From the previous work by Brès,[13] on the subsonic regime ($0.3 \leq M_\infty \leq 0.6$) of cavity flow, it was inferred that mode I dominates the flow behavior in subsonic Mach number regime. However, the present investigation reveals that as we increase M_∞ to the transonic regime, the dominant mode changes from Rossiter mode I to II as seen in Figure 6. This transition indicated by the broken vertical line in Figure 6 occurs at lower Mach number for higher Reynolds number. As shown in Figure 5, the acoustic radiation becomes stronger at M_∞ around 0.8, where the dominant Rossiter mode shifts from I to II. The strong

acoustic wave emission can be correlated with Rossiter mode II, as it can be seen in Figure 7. For flows of $Re_\theta > 46$, we observe that the dominant mode is Rossiter mode II. It can also be seen from this figure that Reynolds number plays a role in switching modes.

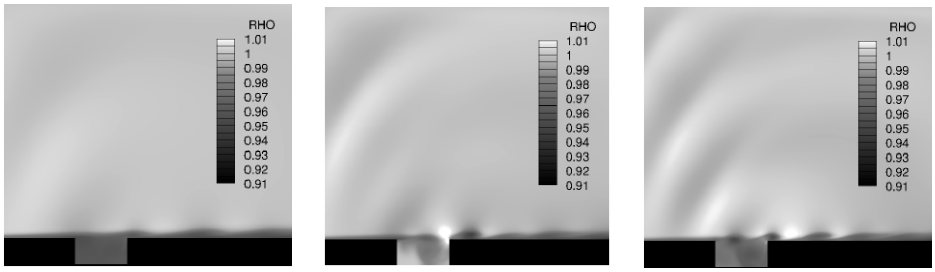

$Re_\theta = 46$ $Re_\theta = 67$ $Re_\theta = 77$

Figure 7: Effect of Reynolds number variation on the flow field for $M_\infty = 0.6$.

An overview of effects of M_∞ and Re_θ on the stability of open-cavity flows for $L/D = 2$ is shown in Figure 8. When Mach number decreases towards the incompressible limit, the flow becomes more stable for a wider range of Reynolds numbers. Meanwhile, in subsonic regime, increase in Mach number destabilizes the flow. However, for flows with Mach numbers higher than 0.6, open-cavity flow exhibits a flattening of the neutral stability curve. Such results have also been observed by Brès and Colonius.[8] In this study, we further observe that as the Mach number increases to the transonic regime, the velocity fluctuation v/U_∞ weakens. This can be noticed from the upward slope of the neutral stability curve across the transonic regime. This destabilization and subsequent stabilization effects of Mach number are also observed by Yamouni.[17]

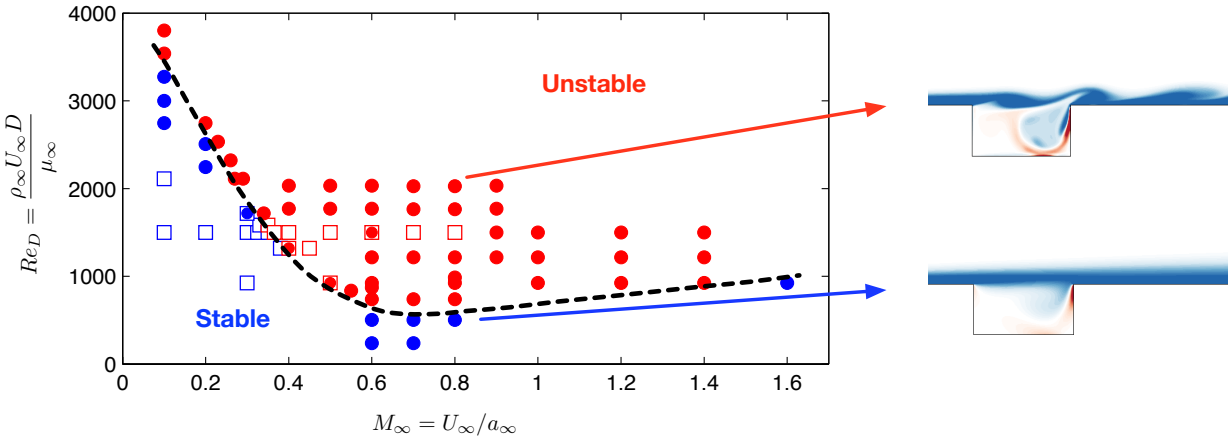

Figure 8: Stability diagram of open-cavity flow for $L/D = 2$. The Red and blue symbols represent the two-dimensional unstable and stable cases, respectively. The open square circles are from Brès and Colonius[8] and the filled circles are from the present study. The black dashed line represents the two-dimensional neutral stability curve. Inserted plots show vorticity contours for representative unstable and stable cases.

Modal Structure Analysis via DMD

We investigate the unstable cases for flow over cavity with $L/D = 2$ to capture the dominant instability modes. We perform dynamic mode decomposition (DMD)[18–20] on cavity flow with $L/D = 2$ to identify the dominant modes and discuss their relationship with the Rossiter modes. This calls for an extraction of the flow features based on frequency content. DMD can decompose the flow structures associated with individual frequencies and identify coherent structures within the flow. For nonlinear flow, the DMD technique provides a linear approximation of the underlying flow.[19] We perform DMD analysis on the flow which is inherently nonlinear for the range of Mach numbers from $M_\infty = 0.6$ to 1.4 for a fixed $Re_\theta = 46$. We collect two periods

of streamwise velocity u, wall normal velocity v and pressure P data, corresponding to dominant frequency obtained from spectral analysis, with a minimum of 45 snapshots per period for all cases considered.

The DMD provides us with the eigenvalue spectra and the corresponding dynamic modes (eigenvectors). We rank these dynamic modes based on their amplitude which corresponds to the norm of the individual modes (eigenvectors). The modal amplitudes represent their individual contribution to the overall energy content. The mode with the highest amplitude for cavity flow corresponds to the mean mode, and the one with the second largest amplitude corresponds to the dominant oscillatory mode in our analysis. As the frequency associated with this dominant mode should be the Rossiter frequency, we first compare in Figure 9 the Strouhal number obtained from DMD analysis with the predictions based on Rossiter's formula.

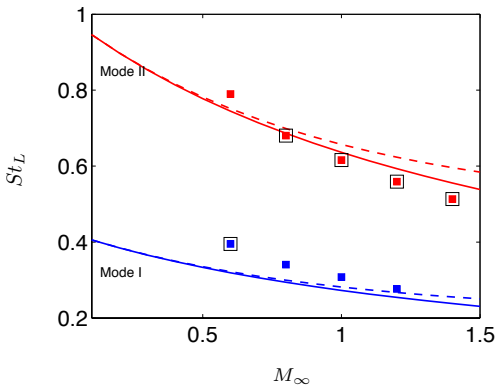

Figure 9: $St_L = fL/U_\infty$ from classic Rossiter semi-empirical (solid line), modified Rossiter formulae (dashed line) from DMD analysis. The blue and red squares represent frequencies corresponding to Rossiter mode I and II, respectively. The open squares indicate the dominant modes.

We observe that the frequencies captured with DMD analysis agree well with the spectral analysis of the probe data obtained in §IIIA. In addition, on ranking the amplitudes, we observe that the frequency corresponding to Rossiter mode I is the dominant frequency for $M_\infty = 0.6$ while for the cases of $M_\infty = 0.8$ to 1.4, the Rossiter mode II is the dominant frequency, consistent with the earlier observations of mode switching. We also obtain the subdominant frequencies for the cases considered with a lower contribution to the overall energy content compared to the dominant mode.

The mean and Rossiter I and II modes are shown for the range of Mach numbers, $M_\infty = 0.6$ to 1.4 in Figures 10 and 11, for streamwise velocity and pressure, respectively. The flow structures in the mean (base) flow are similar to the time-averaged flow field and changes with increasing Mach numbers. The structure of baseline streamwise velocity in Figure 10 within the cavity does not change dramatically with a recirculating region near the cavity trailing edge. For transonic and supersonic flows, compression waves are observed close to the cavity leading edge and shock wave close to the cavity trailing edge in the base pressure contours in Figure 11.

For the subsonic flow of $M_\infty = 0.6$, the pressure contour for Rossiter mode II indicate that the amplitude of pressure is small near the middle of the cavity. Although not shown, a similar inference is obtained for the wall normal velocity contour v. Thus, the spectral analysis performed on v/U_∞ in the middle of the cavity ($x = L/2, y = 0$) does not detect the subdominant Rossiter mode II as seen in Figure 9. We observe from Figures 10 and 11 that as the Mach number increases from the subsonic to the transonic regime, the structures in the shear layer and wake of cavity associated with Rossiter mode I increase in size at a faster rate compared to those associated with Rossiter mode II. For Mach number $M_\infty \approx 1.2$, the size of the shear layer structure for mode I almost occupies the entire cavity length. For higher M_∞, the growth of such structure can no longer be supported over the open cavity. This sub-dominant Rossiter mode I is not observed for $M_\infty = 1.4$ with its energy distributed to the mean and other Rossiter modes. An increase in the structures associated with Rossiter mode II in the cavity shear layer is observed from Figure 11 as the Mach number increases from 0.6 to 1.2. While not shown, this trend is also observed from spectral analysis of probe data from the middle of the cavity ($x = L/2, y = 0$). A compression of the flow field in the upstream direction above the cavity with increasing Mach numbers is observed from the pressure contours and is consistent with the observations in the earlier sections. Interaction of the vortices in the cavity wake with compression

waves are observed in Rossiter mode II for $M_\infty = 1.2$ to 1.4. A pressure oscillation generated at the rear bottom end of the cavity is observed in the Rossiter modes I and II.

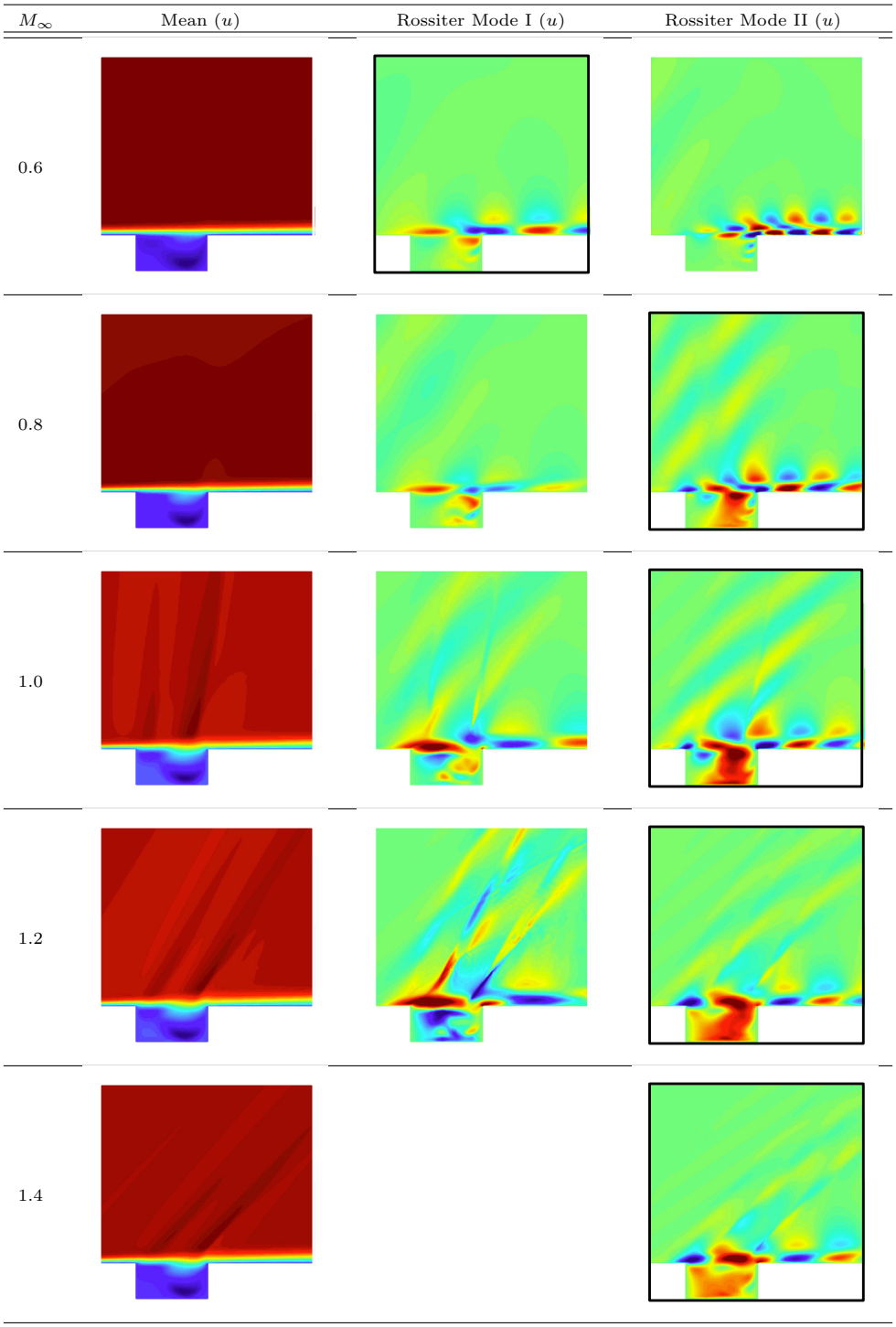

Figure 10: Streamwise velocity contours of the DMD modes corresponding to mean, Rossiter I and II modes with varying Mach numbers for flow over a cavity with $L/D = 2$ and $Re_\theta = 46$. The black boxes indicate the dominant Rossiter mode.

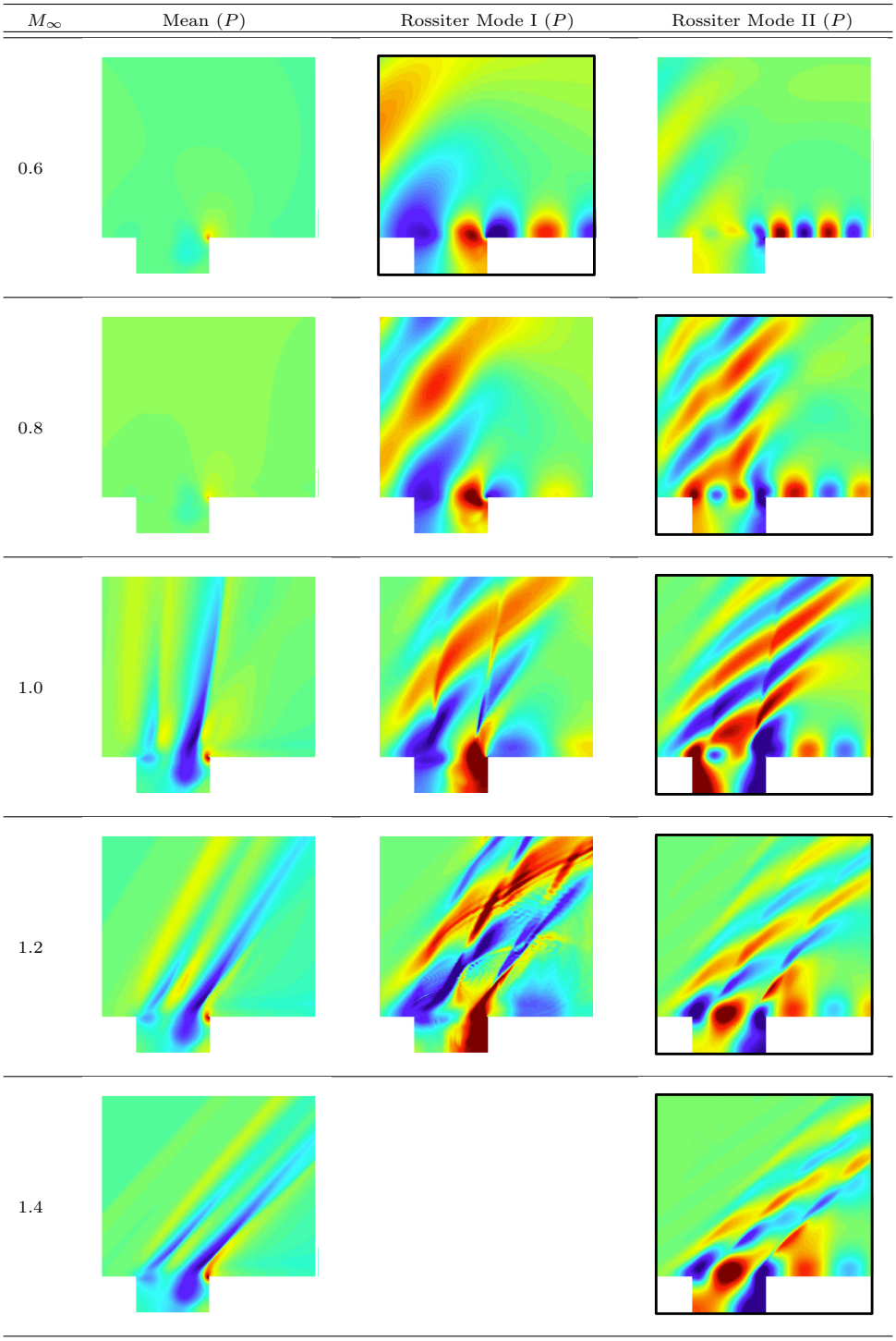

Figure 11: Pressure contours of the DMD modes corresponding to mean, Rossiter I and II modes with varying Mach numbers for flow over a cavity with $L/D = 2$ and $Re_\theta = 46$. The black boxes indicate the dominant Rossiter mode.

B. Flow over cavity of $L/D = 6$

DNS is also performed on the cavity flow with aspect ratio $L/D = 6$ for Mach numbers of 0.1 to 1.2, with lower Re_D from 100 to 1214. Similar analysis to that performed for $L/D = 2$ cavity is conducted to study the effect of Reynolds number and Mach number. Figure 12 shows the flow field of cases with various M_∞ at $Re_\theta = 19$. For the low $M_\infty = 0.3$, we observe the shear layer mode. When M_∞ increases to 0.6, a

large-scale vortex rolls up with an opposite sign vortex sheet being engulfed between the vortices. This type of cavity flow is referred as wake mode by Gharib[21] (for axisymmetric flow). For $M_\infty = 0.9$, the opposite sign vortex patch pulled between the shedding vortices decreases and the amount of fluctuation over the cavity is weakened. Meanwhile, the compression waves are observed at this $M_\infty = 0.9$. As shown in Figure 12, the local Mach number upstream of the trailing edge reaches sonic speeds, and a weak bow shock is formed around the corner which is similar to $L/D = 2$. The acoustic wavelength is almost proportional to the length of cavity. Increasing the Mach number to 1.2, a large recirculation zone is present over the extent of the cavity and the flow becomes stable. A weak Mach wave is formed at the leading edge and shock waves are generated at the trailing edge. We note that increasing Mach number destabilizes the flow in subsonic regime and then stabilizes the flow in transonic regime which agrees with our observations for $L/D = 2$.

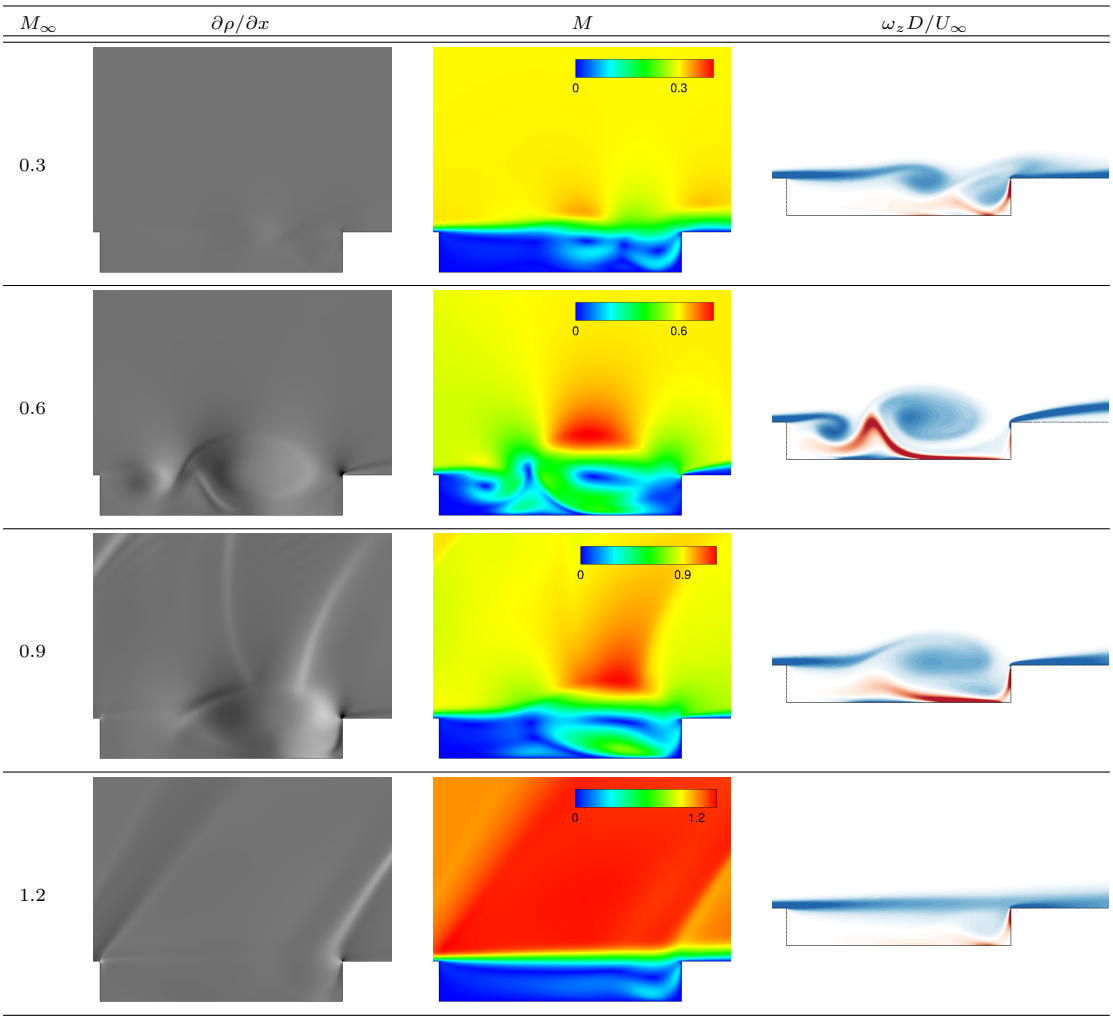

Figure 12: Instantaneous numerical Schilieren ($\partial\rho/\partial x$), local Mach number (M), and vorticity ($\omega_z D/U_\infty$) contours are shown for $M_\infty = 0.3$ to 1.2 and $L/D = 6$ at $Re_\theta = 46$ ($Re_D = 1214$).

In order to characterize the frequency of cavity oscillation for $L/D = 6$, we place three probes tracking velocity (v/U_∞) time history at points ($x/D = 1, y = 0$), ($x/D = 3, y = 0$), ($x/D = 5, y = 0$), respectively. We define the flow over cavity to be stable when all the probe data shows no fluctuations. The Strohual number for $Re_\theta = 10$ and 19 is shown in Figure 13. At $Re_\theta = 10$, the unstable cases show that at different location over the cavity, Rossiter mode II is the dominant mode and the only mode observed. As we increase Re_θ to 19, Rossiter mode I appears along with Rossiter mode II. This is similar to the observations for $L/D = 2$ when Rossiter mode I appears at higher Reynolds number. Thus, increasing Re will induce more Rossiter modes. For comparison, the Strohual number from cavity experiments performed at FSU with $L/D = 6$, $W/D = 3.85$, $Re_D = 3.3 \times 10^5$ (657 times higher than present work) are also plotted in the Figure

13 (right) at $M_\infty = 0.33$ and 0.43. The oncoming flow is turbulent at cavity leading edge in the experiment while it is laminar in present simulations. In experiments, the unsteady wall pressure data is extracted and analyzed at $x/D = 6, y/D = -0.48$. We compare our Rossiter modes results based on probe 3 ($x/D = 5$, $y/D = 0$) which is closest to the probe location in the experiment.

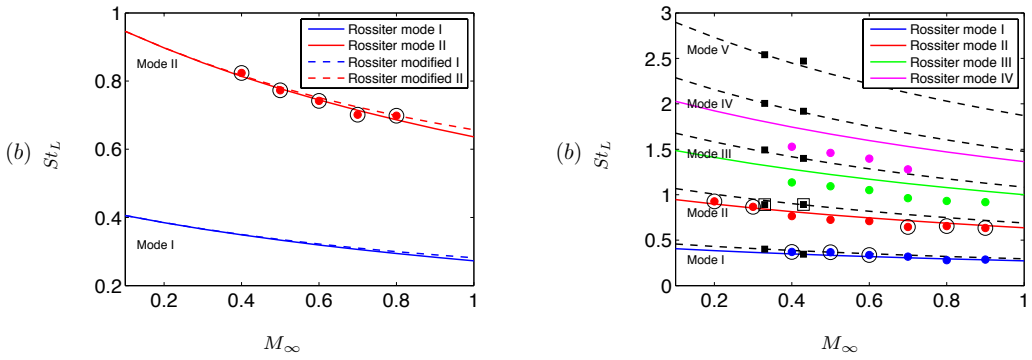

Figure 13: Comparison of $St_L = fL/U_\infty$ from classic Rossiter semi-empirical formula (solid line), modified Rossiter formula (dashed line) and present work for $L/D = 6$ at (a) $Re_\theta = 10$; (b) $Re_\theta = 19$. The blue, red, green and magenta circles represent frequencies corresponding to Rossiter mode I, II, III and IV, respectively ($1/\kappa = 1.75$). The dominant mode is circled in black. The black solid square represents experiments results for $Re_D = 3.3 \times 10^5$ (dashed black line with $1/\kappa = 1.65$) and the dominant mode is represented by open black square.

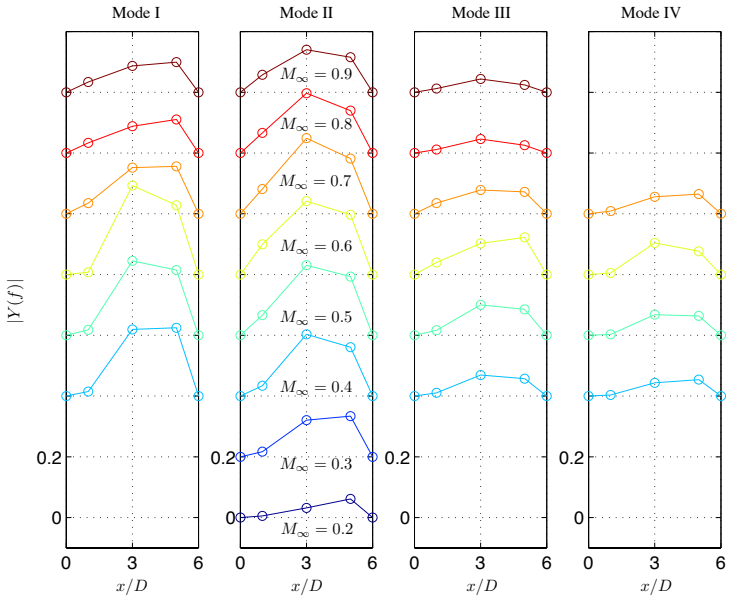

Figure 14: The single-sided amplitude spectra of v/U_∞ for each mode at different Mach number for $L/D = 6$ along streamwise. Individual spectra are shifted by 0.2 in the vertical direction for graphical clarity.

Through spectral analysis for cases with $Re_\theta = 19$, we compare the single-sided amplitudes spectrum $Y(f)$ of velocity tracked by three probes along $y = 0$. Figure 14 exhibits the amplitude of $|Y(f)|$ at the Rossiter frequency at three spatial locations of the probes over the cavity. We find that increasing Mach number (from subsonic to transonic) initially makes the fluctuation larger until $M_\infty = 0.6$. The fluctuation then decreases for higher Mach numbers suggesting stabilization of the flow. This phenomenon is observed for all Rossiter modes existing in the flow field and especially Rossiter modes I and II are the main components of the fluctuation in the shear layer. We also observe that as the shear layer convects from the leading edge, the fluctuation amplifies differently for each Rossiter mode and attains its maximum at different locations

along the cavity length.

We summarize the stability characteristics of the $L/D = 6$ flows. The aforementioned spectral analysis shows that increasing Mach number from subsonic regime destabilizes the flow first and then stabilizes it for higher Mach numbers. This observation is consistent with the neutral stability curve shown in Figure 15. Compared to $L/D = 2$, the neutral stability curve for $L/D = 6$ shifts downward in the cases of larger cavity aspect ratio 6 compared to $L/D = 2$. Simply speaking, the flows over larger aspect ratio are more unstable. This is because for the same Mach number and Reynolds number, the length of cavity provides more space for shear layer to evolve and amplify the disturbance. This shift of neutral stability curve is also observed by Brès in his studies from $L/D = 2$ to 4. Similar to $L/D = 2$ cases, increasing Reynolds number destabilizes the flow. We also observe for $L/D = 6$ that the neutral stability curve moves upward past $M_\infty = 0.6$ into the transonic regime. Currently, DMD analyses are underway to examine the flow over the cavity of $L/D = 6$.

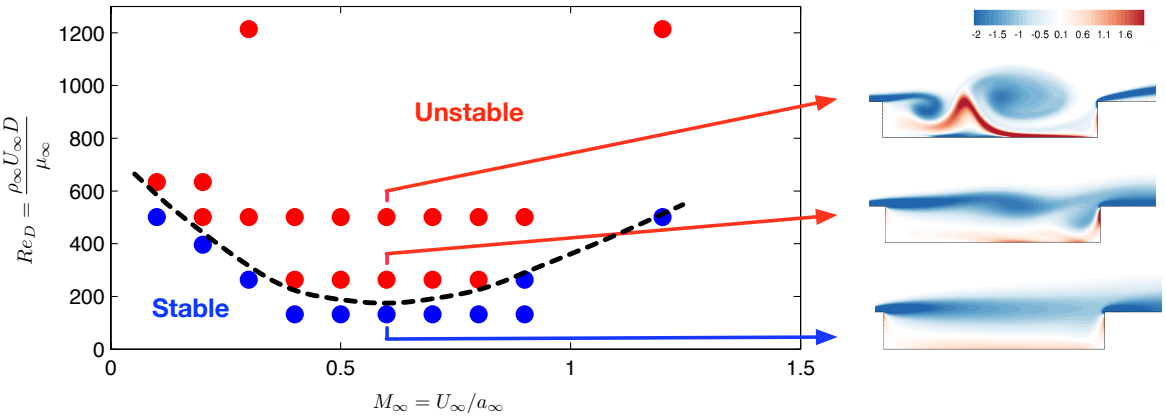

Figure 15: Stability diagram of open-cavity flow for $L/D = 6$. Red and blue symbols represent the two-dimensional unstable and stable cases, respectively. The black line represents two-dimensional neutral stability curve. Inserts show the vorticity plots for representative unstable and stable cases.

IV. Summary

Two-dimensional direct numerical simulations have been performed to examine the effects of Reynolds number and Mach number on open rectangular cavity flow with $L/D = 2$ and 6. In particular, we considered a range of Mach numbers that cover from subsonic to transonic flows ($M_\infty = 0.1$ to 1.6). Building upon the stability map reported by Brès and Colonius,[8] we have extended the neutral stability map to higher Mach numbers. It is observed that the flow becomes unstable for increasing Mach number up to $M_\infty \approx 0.6$. The trend then reverses and shows stabilizing effects for increasing Mach number above 0.6. This influence from compressibility is shared for both $L/D = 2$ and 6 cavity flows. For the higher aspect ratio cavity, the neutral stability curve is positioned at lower Reynolds numbers. The dominant fluctuation observed in the cavity modes correlated with Rossiter modes I and II. As predicted by Rossiter's formula, we have noticed that increasing Mach number lowers the Strouhal number. Reynolds number played a role in altering the transitional Mach number for Rossiter-mode switching. The flow structures related to different oscillation frequencies are also extracted and identified by DMD. The eigenvalues from the DMD analysis agreed well with the oscillation frequency of the cavity flow. The spatial DMD modes were correlated with the Rossiter modes and provided an explanation for how mode transitions take place.

Based on the two-dimensional studies, three-dimensional analysis of open-cavity flows will be performed in upcoming studies. With the findings from this study, we will conduct linear stability analysis of two and three-dimensional transonic open-cavity flows. The aim of the stability analysis is to provide a guideline for developing effective flow control strategies to be performed in FSU's subsonic and UF's supersonic wind tunnels.

Acknowledgments

We thank Mr. Yang Zhang (FSU) for sharing his experimental results for subsonic flow over cavity of $L/D = 6$. This research was supported by the U.S. Air Force Office of Scientific Research (Award Number FA9550-13-1-0091, Program Manager: Dr. Douglas Smith).

References

[1]Rossiter, J. E., "Wind-Tunnel Experiments on the Flow over Rectangular Cavities at Subsonic and Transonic Speeds," Tech. Rep. 3438, Aeronautical Research Council Reports and Memoranda, 1964.

[2]Colonius, T., "An Overview of Simulation, Modeling, and Active Control of Flow/Acoustic Resonance in Open Cavities," AIAA Paper 2001-0076, 2001.

[3]Lawson, S. J. and Barakos, G. N., "Review of numerical simulations for high-speed, turbulent cavity flows," *Prog. Aero. Sci.*, Vol. 47, 2011, pp. 186–216.

[4]Samimy, M., Kim, J. H., Kastner, J., Adamovich, I., and Utkin, Y., "Active control of high-speed and high-Reynolds-number jets using plasma actuators," *J. Fluid Mech.*, Vol. 578, 2007, pp. 305–330.

[5]Cattafesta, L. N., Song, Q., Williams, D. R., Rowley, C. W., and Alvi, F. S., "Active control of flow-induced cavity oscillations," *Prog. Aero. Sci.*, Vol. 44, 2008, pp. 479–502.

[6]Theofilis, V., "Global linear instability," *Annu. Rev. Fluid Mech.*, Vol. 43, 2011, pp. 319–352.

[7]Rowley, C. W., Colonius, T., and Basu, A. J., "On self-sustained oscillations in two-dimensional compressible flow over rectangular cavities," *J. Fluid Mech.*, Vol. 455, 2002, pp. 315–346.

[8]Brès, G. A. and Colonius, T., "Three-dimensional instabilities in compressible flow over open cavities," *J. Fluid Mech.*, Vol. 599, 2008, pp. 309–339.

[9]Schmid, P., Li, L., Juniper, M., and Pust, O., "Applications of the dynamic mode decomposition," *Theoretical and Computational Fluid Dynamics*, Vol. 25, No. 1-4, 2011, pp. 249–259.

[10]Brès, G. A., Nichols, J. W., Lele, S. K., , and Ham, F. E., "Towards Best Practices for Jet Noise Predictions with Unstructured Large Eddy Simulations," 42nd AIAA Fluid Dynamics Conference, AIAA Paper 2012-2965, New Orleans, 2012.

[11]White, F., *Viscous Fluid Flow*, McGraw-Hill, 1991.

[12]Freund, J. B., "Proposed inflow/outflow boundary condition for direct computation of aerodynamic sound," *AIAA J.*, Vol. 35, No. 4, 1997, pp. 740–742.

[13]Brès, G. A., *Numerical simulations of three-dimensional instabilities in cavity flows*, Ph.D. thesis, California Institute of Technology, 2007.

[14]Heller, H. H., Holmes, G., and Cover, E. E., "Flow induced pressure oscillations in shallow cavities," *Journal of Sound and Vibration*, Vol. 18, No. 4, 1971, pp. 545–553.

[15]Krishnamurty, K., *Sound radiation from surface cutouts in high speed flow*, Ph.D. thesis, California Institute of Technology, 1956.

[16]Rowley, C. W., *Modeling, Simulation, and Control of Cavity Flow Oscillations*, Ph.D. thesis, California Institute of Technology, August 2001.

[17]Yamouni, S., Sipp, D., and Jacquin, L., "Interaction between feedback aeroacoustic and acoustic resonance mechanisms in a cavity flow: a global stability analysis," *Journal of Fluid Mechanics*, Vol. 717, No. 134-165, 2012.

[18]Rowley, C. W., Mezić, I., Bagheri, S., and Henningson, D. S., "Spectral analysis of nonlinear flows," *J. Fluid Mech.*, Vol. 641, 2009, pp. 115–127.

[19]Schmid, P. J., "Dynamic mode decomposition of numerical and experimental data," *J. Fluid Mech.*, Vol. 656, 2010, pp. 5–28.

[20]Mezić, I., "Analysis of Fluid Flows via Spectral Properties of the Koopman Operator," *Annu. Rev. Fluid Mech.*, Vol. 45, No. 3, 2012, pp. 57–78.

[21]Gharib, M., "Response of the cavity shear layer oscillations to external forcing," *AIAA J.*, Vol. 25, No. 1, 1987, pp. 43–47.

Appendix

Table 1: Parameter settings considered for open-cavity flows of $L/D = 2$. Abbreviations for stability are: S = Stable; U = Unstable.

Cases	Parameters					Stability
	L/D	M_∞	D/θ_0	Re_θ	Re_D	Nonlinear (2D)
2M01Re104	2	0.1	26.4	104	2746	S
2M01Re114	2	0.1	26.4	114	3000	S
2M01Re124	2	0.1	26.4	124	3274	S
2M01Re134	2	0.1	26.4	134	3538	U
2M01Re144	2	0.1	26.4	144	3802	U
2M02Re85	2	0.2	26.4	85	2244	S
2M02Re95	2	0.2	26.4	95	2708	S
2M02Re104	2	0.2	26.4	104	2746	U
2M023Re96	2	0.23	26.4	96	2534	U
2M026Re88	2	0.26	26.4	88	2323	U
2M027Re80	2	0.27	26.4	80	2112	U
2M029Re80	2	0.29	26.4	80	2112	U
2M03Re65	2	0.3	26.4	65	1716	S
2M034Re65	2	0.34	26.4	65	1716	U
2M04Re50	2	0.4	26.4	50	1320	U
2M04Re67	2	0.4	26.4	67	1769	U
2M04Re77	2	0.4	26.4	77	2033	U
2M05Re35	2	0.5	26.4	35	924	U
2M05Re67	2	0.5	26.4	67	1769	U
2M05Re77	2	0.5	26.4	77	2033	U
2M055Re33	2	0.55	26.4	33	871	U
2M06Re9	2	0.6	26.4	9	238	S
2M06Re19	2	0.6	26.4	19	502	S
2M06Re28	2	0.6	26.4	28	739	U
2M06Re33	2	0.6	26.4	33	871	U
2M06Re35	2	0.6	26.4	35	924	U
2M06Re46	2	0.6	26.4	46	1214	U
2M06Re56.8	2	0.6	26.4	56.8	1500	U
2M06Re67	2	0.6	26.4	67	1769	U
2M06Re77	2	0.6	26.4	77	2033	U
2M07Re9	2	0.7	26.4	9	238	U
2M07Re19	2	0.7	26.4	19	502	U
2M07Re28	2	0.7	26.4	28	739	U
2M07Re46	2	0.7	26.4	46	1214	U
2M07Re67	2	0.7	26.4	67	1769	U
2M07Re77	2	0.7	26.4	77	2033	U
2M08Re19	2	0.8	26.4	19	502	S
2M08Re28	2	0.8	26.4	28	739	U
2M08Re35	2	0.8	26.4	35	924	U
2M08Re37	2	0.8	26.4	37	986	U
2M08Re46	2	0.8	26.4	46	1214	U
2M08Re67	2	0.8	26.4	67	1769	U
2M08Re77	2	0.8	26.4	77	2033	U
2M09Re46	2	0.9	26.4	46	1214	U
2M09Re56.8	2	0.9	26.4	56.8	1500	U
2M09Re67	2	0.9	26.4	67	1769	U
2M09Re77	2	0.9	26.4	77	2033	U
2M1Re35	2	1.0	26.4	35	924	U
2M1Re46	2	1.0	26.4	46	1214	U
2M1Re56.8	2	1.0	26.4	56.8	1500	U
2M12Re35	2	1.2	26.4	35	924	U
2M12Re46	2	1.2	26.4	46	1214	U
2M12Re56.8	2	1.2	26.4	56.8	1500	U
2M14Re35	2	1.4	26.4	35	924	U
2M14Re46	2	1.4	26.4	46	1214	U
2M14Re56.8	2	1.4	26.4	56.8	1500	U
2M16Re35	2	1.6	26.4	35	924	S

Table 2: Parameter settings considered for open-cavity flows of $L/D = 6$. Abbreviations for stability are: S = Stable; U = Unstable.

Cases	Parameters					Stability
	L/D	M_∞	D/θ_0	Re_θ	Re_D	Nonlinear (2D)
6M04Re5	6	0.4	26.4	5	132	S
6M05Re5	6	0.5	26.4	5	132	S
6M06Re5	6	0.6	26.4	5	132	S
6M07Re5	6	0.7	26.4	5	132	S
6M08Re5	6	0.8	26.4	5	132	S
6M09Re5	6	0.9	26.4	5	132	S
6M03Re10	6	0.3	26.4	10	264	S
6M04Re10	6	0.4	26.4	10	264	U
6M05Re10	6	0.5	26.4	10	264	U
6M06Re10	6	0.6	26.4	10	264	U
6M07Re10	6	0.7	26.4	10	264	U
6M08Re10	6	0.8	26.4	10	264	U
6M09Re10	6	0.9	26.4	10	264	S
6M02Re15	6	0.2	26.4	15	396	S
6M01Re19	6	0.1	26.4	19	502	S
6M02Re19	6	0.2	26.4	19	502	U
6M03Re19	6	0.3	26.4	19	502	U
6M04Re19	6	0.3	26.4	19	502	U
6M05Re19	6	0.5	26.4	19	502	U
6M06Re19	6	0.6	26.4	19	502	U
6M07Re19	6	0.7	26.4	19	502	U
6M08Re19	6	0.8	26.4	19	502	U
6M09Re19	6	0.9	26.4	19	502	U
6M12Re19	6	1.2	26.4	19	502	S
6M01Re24	6	0.1	26.4	24	634	U
6M02Re24	6	0.2	26.4	24	634	U
6M03Re46	6	0.3	26.4	46	1214	U
6M12Re46	6	1.2	26.4	46	1214	U